

Model of the polarized foreground diffuse Galactic emissions from 33 to 353 GHz

L. Fauvet, J. F. Macías-Pérez

LPSC, Université Joseph Fourier Grenoble 1, CNRS/IN2P3, Institut National Polytechnique de Grenoble, 53 avenue des Martyrs, 38026 Grenoble cedex, France

F.X. Désert

IPAG: Institut de Planétologie et d'Astrophysique de Grenoble, UJF-Grenoble 1 / CNRS-INSU, UMR 5274, Grenoble, F-38041, France

Abstract

We present 3D models of the Galactic magnetic field including regular and turbulent components, and of the distribution of matter in the Galaxy including relativistic electrons and dust grains. By integrating along the line of sight, we construct maps of the polarized Galactic synchrotron and thermal dust emissions for each of these models. We perform a likelihood analysis to compare the maps of the Ka, Q, V and W bands of the Wilkinson Microwave Anisotropy Probe (WMAP) and the 353 GHz ARCHEOPS data to the models obtained by varying the pitch angle of the regular magnetic field, the relative amplitude of the turbulent magnetic field and the extrapolation spectral indices of the synchrotron and thermal dust emissions. The best-fit parameters obtained for the different frequency bands are very similar and globally the data seem to favor a negligible isotropic turbulent magnetic field component at large angular scales (an anisotropic line-of-sight ordered component can not be studied using these data). From this study, we conclude

that we are able to propose a consistent model of the polarized diffuse Galactic synchrotron and thermal dust emissions in the frequency range from 33 to 353 GHz, where most of the CMB studies are performed and where we expect a mixture of these two main foreground emissions. This model can be very helpful to estimate the contamination by foregrounds of the polarized CMB anisotropies, for experiments like the PLANCK satellite.

Keywords: ISM: general – Methods: data analysis – Cosmology: observations – millimeter

1. Introduction

The PLANCK¹ satellite mission (Planck-Collaboration (2011a); Tauber et al. (2010)), currently in flight, will provide measurements of the CMB anisotropies both in temperature and polarization over the full sky with an unprecedented accuracy (Planck-Collaboration, 2005). In particular, it should be able to measure the tensor-to-scalar ratio, r , which sets the energy scale of inflation (Lyth (1984); Peiris et al. (2003)). For an extended mission and in the case of no direct detection, Planck should set an upper limit of $r < 0.03$ (Burigana et al., 2010; Efstathiou et al., 2009; Efstathiou and Gratton, 2009), and thus provides tight constraints on inflationary models (Baumann (2009)). To achieve this high level of sensitivity, it is necessary to estimate accurately the temperature and polarization anisotropies from foreground diffuse Galactic emissions and from point-like and compact sources of Galactic and extraGalactic origin. A reliable estimation of the residual contamination due to the foreground emissions after application of component separation

¹<http://www.rssd.esa.int/index.php?project=Planck>

methods (see Betoule et al. (2009); Leach et al. (2008) for recent studies) is thus necessary to retrieve the cosmological information from the PLANCK data.

As summarized in Fauvet et al. (2011) the main polarized foreground contributions come from the diffuse Galactic synchrotron emission (Page et al., 2007) and from thermal dust emission (Benoît et al., 2004; Ponthieu et al., 2005). The polarized synchrotron emission have already been modelled by Page et al. (2007); Sun et al. (2008); Jaffe et al. (2010); Jansson et al. (2009); Fauvet et al. (2011) based on models of the Galactic magnetic field (Han et al., 2004, 2006) and of the relativistic electrons in the Galaxy. Concerning the thermal dust emission, modeling based on the physical origins of this polarized emission has already been discussed in Ponthieu et al. (2005); Page et al. (2007); Fauvet et al. (2011).

We propose here an extended analysis of the 3D joint model of the Galactic polarized diffuse emissions discussed in Fauvet et al. (2011). In the previous analysis we focused on the WMAP data at 23 GHz and ARCHEOPS at 353 GHz data where synchrotron and thermal dust emissions dominate, respectively. Here, we use complementary data : the other frequency bands of WMAP from 33 to 94 GHz, where a mixing of those emissions is expected, and the ARCHEOPS data at 353 GHz. Furthermore we apply here a pixel-to-pixel likelihood based comparison instead of a Galactic profile-based method as discussed in Fauvet et al. (2011).

The paper is structured as follows: Sect. 2 describes the five-year WMAP and ARCHEOPS data set used in the analysis. In Sect.3 we describe in detail models for the polarized foreground emissions. Section 4 discusses the 3D model of the Galaxy using to construct the polarized Galactic emissions. The models are statistically compared to the data in Section 5 and we discuss the results in Section 6. We finally conclude in Section 7.

2. Observations

2.1. *Diffuse Galactic synchrotron emission*

The synchrotron emission is an important contributor to the diffuse sky emission at both radio and microwave observation frequencies.

In intensity, the 408MHz all-sky continuum survey (Haslam et al. (1982)), at a resolution of 0.85 degrees, is a good tracer of the synchrotron emission and it will be used in the following as a template. In particular, we use the 408MHz all-sky map available on the LAMBDA website in the HEALPIX pixelisation scheme (Gòrski et al., 2005). We correct this map from the contribution from free-free emission which estimated to be about 30 %. The corrected maps was then downgraded to the resolution of the WMAP and Archeops maps discussed below.

In polarization, Faraday rotation introduces complications into the interpretation of the radio data since strong depolarization is observed for frequencies lower than 10 GHz, particularly concerning the inner part of the Galaxy (Burn (1966); Sun et al. (2008); Jaffe et al. (2010); Jansson et al. (2009);

La Porta et al. (2006)). A detailed discussion on the depolarization process, based on data from the Leiden survey, can be found in La Porta and Burigana (2006). For this reason the best polarized Galactic diffuse synchrotron tracers are at high frequency such as the WMAP survey (Page et al. (2007)).

We used here the five-year WMAP Q and U low resolution maps for the frequency channels centered at 33 (Ka band), 41 (Q band), 61 (V band) and 94 GHz (W band) (Page et al. (2003); Gold et al. (2009)). These data are available on the LAMBDA website in the HEALPIX pixelisation scheme at $N_{side} = 16$. The associated noise is estimated using the full noise correlation matrix also available on the LAMBDA website in the same resolution.

2.2. Thermal dust

The thermal dust emission is significant in the WMAP data only for frequencies above 70 GHz, then we also used here the ARCHEOPS 353 GHz Q and U maps as tracers of the polarized thermal dust emission. Those maps cover about 20 % of the sky (Macías-Pérez et al., 2007) and were filtered and downgraded to $N_{side} = 16$ to make them comparable to the WMAP ones.

In intensity, the most accurate measurements of the thermal dust emission are those of the IRAS satellite (Neugebauer et al., 1984) and in particular at 100 μm . We use here predicted full-sky maps of sub millimeter and microwave emission from the diffuse interstellar dust in the Galaxy from Finkbeiner et al. (1999) which were produced combining the IRAS data at 6.1 arcmin and the COBE DIRBE data at 40 arcmin (Schlegel et al., 1998). These maps were downgraded to the resolution of the WMAP and Archeops

maps presented above.

3. Emissivity model in polarization

We present in this section a realistic model of the diffuse polarized synchrotron and dust emissions using a 3D model of the Galactic magnetic field and of the matter density in the Galaxy. We will consider the distribution of relativistic cosmic-ray electrons (CREs), n_{CRE} , for the synchrotron emission and the distribution of dust grains, n_{dust} , for the thermal dust emission. Following Fauvet et al. (2011) we calculate the Stokes parameters I, Q and U for the Galactic polarized emission along the line of sight as follows.

For the synchrotron emission (Rybicki and Lightman (1979)) we write :

$$I_{\nu}^{\text{sync}}(\mathbf{n}) = I_{\text{Has/ff}}(\mathbf{n}) \left(\frac{\nu}{0.408} \right)^{\beta_s}, \quad (1)$$

$$Q_{\nu}^{\text{sync}}(\mathbf{n}) = I_{\text{Has/ff}}(\mathbf{n}) \left(\frac{\nu}{0.408} \right)^{\beta_s} \quad (2)$$

$$\frac{\int \cos(2\gamma(\mathbf{n}, s)) p_s (B_l^2(\mathbf{n}, s) + B_t^2(\mathbf{n}, s)) n_{\text{CRE}}(\mathbf{n}, s) ds}{\int (B_l^2(\mathbf{n}, s) + B_t^2(\mathbf{n}, s)) n_{\text{CRE}}(\mathbf{n}, s) ds}, \quad (3)$$

$$U_{\nu}^{\text{sync}}(\mathbf{n}) = I_{\text{Has/ff}}(\mathbf{n}) \left(\frac{\nu}{0.408} \right)^{\beta_s} \quad (4)$$

$$\frac{\int \sin(2\gamma(\mathbf{n}, s)) p_s (B_l^2(\mathbf{n}, s) + B_t^2(\mathbf{n}, s)) n_{\text{CRE}}(\mathbf{n}, s) ds}{\int (B_l^2(\mathbf{n}, s) + B_t^2(\mathbf{n}, s)) n_{\text{CRE}}(\mathbf{n}, s) ds}, \quad (5)$$

where $B_n(\mathbf{n}, s)$ is the magnetic component along the line-of-sight \mathbf{n} , and $B_l(\mathbf{n}, s)$ and $B_t(\mathbf{n}, s)$ the magnetic field components on a plane perpendicular to the line-of-sight. Notice that the 3 vectors n, l, t form an orthonormal basis being l and t oriented to the north and to the east respectively in a plane perpendicular to n . The polarization fraction p_s is set to 75% (Rybicki and Lightman, 1979). The polarization angle $\gamma(\mathbf{n}, s)$ is given by :

$$\gamma(\mathbf{n}, s) = \frac{1}{2} \arctan \left(\frac{2B_l(\mathbf{n}, s) \cdot B_t(\mathbf{n}, s)}{B_l^2(\mathbf{n}, s) - B_t^2(\mathbf{n}, s)} \right). \quad (6)$$

The distribution of relativistic electrons, n_{CRE} , is described in detail in section 4. $I_{\text{Has/ff}}$ is the reference map in intensity constructed from the *408 MHz all sky continuum survey* Haslam et al. (1982) after subtraction of the bremsstrahlung (*free-free*) emission and ν is the frequency of observation. To subtract the free-free contribution we used the WMAP K-band free-free foreground map generated from the maximum entropy method (MEM) (Hinshaw et al., 2007; Bennett et al., 2003). Notice that we do not use the synchrotron MEM intensity map at 23 GHz (Hinshaw et al. (2007)) as a synchrotron template to avoid any possible Anomalous Microwave Emission (AME) contamination (the WMAP team made no attempt to fit for the latter). The spectral index β_s used to extrapolate maps at various frequencies is a free parameter of the model. **The SED of the synchrotron emission in the radio and microwave domain, and in particular in the 33 to 353 GHz range, can be well approximated by a power law in antenna temperature units (Rybicki and Lightman (1979)). This is due to the fact that the energy spectrum of the Galactic relativistic electrons producing the radio and microwave synchrotron emission is also well approximated by a power law (Kobayashi et al. (2004)).**

For the thermal dust emission we write

$$I_{\nu}^{\text{dust}}(\mathbf{n}) = I_{\text{fds}}(\mathbf{n}) \left(\frac{\nu}{353} \right)^{\beta_d}, \quad (7)$$

$$Q_{\nu}^{\text{dust}}(\mathbf{n}) = I_{\text{fds}}(\mathbf{n}) \left(\frac{\nu}{353} \right)^{\beta_d} \quad (8)$$

$$\frac{\int \cos(2\gamma(\mathbf{n}, s)) \sin^2(\alpha) f_{\text{norm}} p_d n_{\text{dust}}(\mathbf{n}, s) ds}{\int n_{\text{dust}}(\mathbf{n}, s) ds}, \quad (9)$$

$$U_{\nu}^{\text{dust}}(\mathbf{n}) = I_{\text{fds}}(\mathbf{n}) \left(\frac{\nu}{353} \right)^{\beta_d} \quad (10)$$

$$\frac{\int \sin(2\gamma(\mathbf{n}, s)) \sin^2(\alpha) f_{\text{norm}} p_d n_{\text{dust}}(\mathbf{n}, s) ds}{\int n_{\text{dust}}(\mathbf{n}, s) ds}, \quad (11)$$

where the dust polarization fraction p_d is set to 10 % (Ponthieu et al., 2005) based on the ARCHEOPS data, and $n_{\text{dust}}(r, z)$ is the dust grain distribution discussed in section 4. The $\sin^2(\alpha)$ term accounts for the geometrical suppression and f_{norm} is an empirical factor which accounts for the misalignment between dust grains and the magnetic field lines (see (Fauvet et al., 2011) for details). The reference map, I_{fds} was taken to be model 8 in Finkbeiner et al. (1999) at 545 GHz. The spectral index β_d used to extrapolate maps at various frequencies is a free parameter of the model. In the following we work on antenna temperature, Rayleigh-Jeans units. Assuming nearly constant dust temperature across the sky then a power-law approximation for the thermal dust emission in antenna temperature units can be used (Planck-Collaboration, 2011c).

4. A 3D modeling of the Galaxy

We describe here the 3D model of the Galaxy as used in the previous Stokes parameter definitions both for synchrotron and dust.

4.1. Matter density model

In galactocentric cylindrical coordinates (r, z, ϕ) we consider an exponential distribution of relativistic electrons n_{CRE} on the Galactic disk motivated by Drimmel and Spergel (2001):

$$n_{CRE}(r, z) = n_{0,e} \cdot \frac{e^{-\frac{r}{n_{CRE,r}}}}{\cosh 2(z/n_{CRE,h})}, \quad (12)$$

where $n_{CRE,h}$ defines the width of the distribution vertically and it is set to 1 kpc in the following. $n_{CRE,r}$ defines the distribution radially and it is set to 3 kpc (see Sun et al. (2008); Jaffe et al. (2010); Fauvet et al. (2011)). The value of $n_{0,e}$ is set to $6.4 \times 10^{-6} \text{ cm}^{-3}$ (Sun et al., 2008).

The density distribution of dust grains in the Galaxy is poorly known and we therefore choose to describe it in the same way as for relativistic electrons:

$$n_d(r, z) = n_{0,d} \cdot \frac{e^{-\frac{r}{n_{d,r}}}}{\cosh 2(z/n_{d,h})}, \quad (13)$$

where $n_{d,r}$ and $n_{d,h}$ are the radial and vertical widths of the distribution. In the following we set them to 3 and 1 kpc respectively. Notice that we expect these two parameters to be strongly correlated for both dust grain and electron distributions, hence we decided to fix one of them as in previous analyses (Sun et al. (2008); Jaffe et al. (2010)). We have tested different values of these two parameters and found no impact on the final results.

4.2. Galactic magnetic field model

The Galactic magnetic field model consists of a regular component and a turbulent component such that

$$\mathbf{B}_{tot}(\mathbf{r}) = \mathbf{B}_{reg}(\mathbf{r}) + A_{turb} \mathbf{B}_{turb}(\mathbf{r}) \quad (14)$$

where A_{turb} is the amplitude of the turbulent component and it is a free parameter of the model. In the following we will express it as a relative amplitude with respect to the amplitude of the regular component.

4.2.1. Regular component

The regular part $\mathbf{B}_{reg}(\mathbf{r})$ is a Modified Logarithmic Spiral model, discussed in detail in Fauvet et al. (2011). In galactocentric cylindrical coordinates (r, ϕ, z) it reads

$$\begin{aligned} \mathbf{B}(\mathbf{r}) = & B_{reg}(\mathbf{r}) [\cos(\phi + \beta) \ln \left(\frac{r}{r_0} \right) \sin(p) \cos(\chi) \cdot \mathbf{u}_r \\ & - \cos(\phi + \beta) \ln \left(\frac{r}{r_0} \right) \cos(p) \cos(\chi) \cdot \mathbf{u}_\phi \\ & + \sin(\chi) \cdot \mathbf{u}_z], \end{aligned} \quad (15)$$

where p is the pitch angle, $\beta = 1/\tan(p)$ and r_0 is the radial scale set to 7.1 kpc. $\chi(r) = \chi_0(r)(z/z_0)$ is the vertical scale, with $\chi_0 = 22.4$ degrees and $z_0 = 1$ kpc. Following Taylor and Cordes (1993) we restrict our model to the range $3 < r < 20$ kpc. The lower limit is set to avoid the center of the Galaxy for which the physics is poorly constrained and the model diverges. The intensity of the regular field is fixed using pulsar Faraday

rotation measurements by Han et al. (2006)

$$B_{reg}(r) = B_0 e^{-\frac{r-R_\odot}{R_B}} \quad (16)$$

where the large-scale field intensity at the Sun position is $B_0 = 2.1 \pm 0.3 \mu G$ and the physical cut $R_B = 8.5 \pm 4.7$ kpc. The distance between the Sun and the Galactic center, R_\odot is set to 8 kpc (Eisenhauer et al. (2003); Reid and Brunthaler (2005)).

4.2.2. Turbulent component

In addition to the large-scale Galactic magnetic field, Faraday rotation measurements on pulsars in our vicinity have revealed a turbulent component on scales smaller than a few hundred pc (Lyne and Smith (1989)). Moreover it seems to be present on large angular scales (Han et al. (2004)) with an amplitude estimated to be of the same order of magnitude as that of the regular one (Han et al. (2006)). The magnetic energy in Fourier space, $E_B(k)$, associated with the turbulent component is well described by a power spectrum of the form (Han et al. (2004, 2006))

$$E_B(k) = C \left(\frac{k}{k_0} \right)^\alpha \quad (17)$$

where $\alpha = -0.37$ and $C = (6.8 \pm 0.3) \cdot 10^{-13} \text{ erg cm}^{-3} \text{ kpc}$. To obtain the 3D spatial distribution of the turbulent magnetic field we produced independent Gaussian simulations from the above power spectrum in the x , y and z directions on boxes of 512^3 pixels at a resolution of 56 pc. We renormalize the simulated boxes so that the total amplitude of the turbulent component is A_{turb} .

Notice that we do not include here an anisotropic/ordered component as discussed in Jaffe et al. (2010). As in (Fauvet et al., 2011), our regular component is then equivalent to the sum of what Jaffe et al. (2010) call the coherent and ordered fields. The latter, also called ordered random component, will be not considered in this paper because it can not be distinguished from the large-scale magnetic field when studying polarization intensity only.

5. Method

We compute I, Q and U maps for the synchrotron and thermal dust emissions with a modified version of the HAMMURABI code (Waelkens et al. (2009)). Each map is generated by integrating in 100 steps along each line-of-sight defined by the HEALPIX (Górski et al., 2005) $N_{\text{side}} = 16$ pixel centres. The integration continues out to 25 kpc from the observer situated 8.5 kpc from the Galactic centre. These full-sky maps are computed for a grid of models obtained by varying the pitch angle, p , the turbulent component amplitude, A_{turb} and the spectral indices of the synchrotron and thermal dust emissions β_s and β_d . The latter are assumed to be spatially constant on the sky. Dealing with a more realistic varying spectral index (see Kogut et al. (2007); La Porta et al. (2008) for detailed studies) is beyond the scope of this paper. However, we ensured that this hypothesis does not impact the results for the other free parameters in the model. Indeed, we produced simulated WMAP observations with spatially varying synchrotron spectral index and analyzed them assuming a constant one. No significant bias was observed for any of the other parameters and the error bars were equivalent to those

Table 1: Parameters of the 3D Galactic diffuse emissions model.

Parameter	Range	Binning
p (deg)	$[-80.0, 15.0]$	5.0
β_s	$[-4.5, -2.8]$	0.05
β_d	$[0.05, 2.5]$	0.05
A_{turb}	$[0.1, 1.1] * B_{reg}$	0.1

in the case of a constant spectral index.

The range and binning step considered for each of the above parameters are given in Table 1. All the other parameters of the models of the Galactic magnetic field and matter density are fixed to values proposed in Section 4. Notice that to be able to compare the dust models to the ARCHEOPS 353 GHz data, the simulated maps are multiplied by a mask to account for the ARCHEOPS partial sky coverage of 30% (Macías-Pérez et al., 2007).

5.1. Likelihood based analysis

To compare the WMAP data sets and the model of Galactic polarized emissions we used a maximum likelihood analysis where the the log-likelihood function is given by

$$-\log \mathcal{L}_\nu = \sum_i \sum_{j=0}^{N_{\text{pix}}-1} (D_{i,j}^\nu - M_{i,j}^\nu) N_{\text{inv},\nu}^{-1} (D_{i,j}^\nu - M_{i,j}^\nu) \quad (18)$$

where $D_{i,j}^\nu$ and $M_{i,j}^\nu$ correspond respectively to the data set and model for the

frequency of observation ν . i and j index the polarization states Q and U and the pixel number in the maps respectively. $N_{\text{inv},\nu}^{-1}$ is the pixel-to-pixel inverse covariance matrices for the frequency band ν . These matrices allow us to estimate the noise for a given pixel and the correlation between pixels. They are composed of 6144×6144 elements allocated in 4 blocks of 3072×3072 elements each. Each element represents the auto-correlated noise associated to a pixel or the correlation between 2 pixels. The elements linked to the pixel located outer the processing mask are set to 0 (Hinshaw et al., 2009; Limon et al., 2009). These matrices are available on the LAMBDA website.²

We used the processing mask of the WMAP team. This processing mask is built from intensity cuts on the WMAP polarized maps at 23 GHz and the thermal dust emission model of the WMAP team (Kogut et al., 2007; Page et al., 2007). The point-sources have also been subtracted. More details concerning this mask can be found in Hinshaw et al. (2009); Limon et al. (2009).

We also used a maximum likelihood analysis to compare the thermal dust emission model to the ARCHEOPS data. The log-likelihood function is defined by

$$-\log \mathcal{L} = \sum_i \sum_{j=0}^{N_{\text{pix}}-1} \frac{(D_{i,j} - M_{i,j})(D_{i,j} - M_{i,j})}{\sigma^2_{i,j}} \quad (19)$$

where $D_{i,j}^\nu$ and $M_{i,j}^\nu$ correspond to the ARCHEOPS data and to the thermal

²<http://lambda.gsfc.nasa.gov/product/map/current/>

dust emission model at 353 GHz. i and j index the Stokes parameters Q and U and the pixel number respectively. The error bars associated to the ARCHEOPS data are estimated from 600 simulations of the time ordered data (TOD) (see Ponthieu et al. (2005); Macías-Pérez et al. (2007)). The instrumental noise at the TOD level was estimated following Benoît et al. (2003). From these simulations we conclude that the noise in the Archeops maps can be well approximated by anisotropic white noise on the maps. We thus compute the variance per pixel.

6. Results

First of all, we consider a null turbulent magnetic field component. For this case, the constraints on the parameters of the polarized Galactic emission model, β_s , β_d and p , using the WMAP and Archeops data are presented in Table 2. For illustration, we also present on Figure 1 the combined marginalized likelihood at 1 and 2D using all the WMAP data. We present the 68.8% (black), 95.4% (dark grey) and 98% (grey) confidence level contours. The pitch angle, p , of the regular magnetic field component does not seem to be correlated neither with β_s nor β_d . Similar results are found in the case of the Archeops data. The best-fit values obtained for magnetic field pitch angle, p , are compatible for the WMAP and ARCHEOPS data, indicating that the same magnetic field can describe both emissions. For β_d , as it might be expected, constraints are only reliable at high frequency (94 and 353 GHz) and are compatible within the $1\text{-}\sigma$ error bars. These results are also compatible at 1σ level with results presented in Boulanger et al. (1996); Gold et al. (2009). Notice that the value obtained is for a fix degree of polarization. An independent

Table 2: Best-fit parameters for the models of the Galactic polarized emissions including a MLS Galactic magnetic field, constrained using the WMAP and ARCHEOPS data inner and outer the P06 mask. The χ^2 are given by degree of freedom

Frequency band	zone	$p(deg)$	β_s	β_d	χ^2_{min}
Ka	in P06	-30.0^{+13}_{-20}	-3.45 ± 0.5	$0.5^{+0.3}_{-0.1}$	10.09
	out of P06	-35.0^{+10}_{-15}	$-3.5^{+0.05}_{-0.65}$	$0.5^{+0.9}_{-0.15}$	2.89
	all-sky	-35.0^{+20}_{-25}	$-3.45^{+0.05}_{-0.8}$	$0.45^{+0.9}_{-0.25}$	10.08
Q	in P06	-30.0^{+25}_{-20}	$-3.45^{+0.05}_{-0.8}$	$0.8^{+0.8}_{-0.2}$	3.65
	out of P06	-30.0^{+20}_{-15}	$-3.65^{+0.25}_{-0.05}$	$0.8^{+0.7}_{-0.4}$	1.58
	all-sky	-30.0^{+20}_{-15}	$-3.45^{+0.2}_{-0.7}$	$0.8^{+1.3}_{-0.2}$	3.67
V	in P06	-15.0^{+10}_{-17}	$-3.4^{+0.15}_{-0.8}$	$1.25^{+0.9}_{-0.4}$	1.26
	out of P06	-5.0^{+5}_{-40}	$-3.95^{+0.7}_{-0.4}$	$1.8^{+0.3}_{-0.9}$	1.07
	all-sky	-15.0^{+10}_{-25}	$-3.4^{+0.15}_{-0.85}$	$1.25^{+0.7}_{-0.8}$	1.26
W	in P06	-60.0^{+35}_{-15}	$-3.2^{+0.15}_{-1.0}$	$1.56^{+1.05}_{-0.15}$	1.32
	out of P06	-35.0^{+30}_{-25}	$-3.7^{+0.2}_{-0.6}$	$2.15^{+0.25}_{-0.05}$	1.2
	all-sky	-60.0^{+30}_{-15}	$-3.2^{+0.2}_{-1.0}$	$1.5^{+0.7}_{-0.6}$	1.32
all WMAP bands	all-sky	-30.0^{+25}_{-10}	$-3.45^{+0.1}_{-0.4}$	$1.0^{+0.9}_{-0.2}$	16.30
ARCHEOPS 353 GHz	30 % sky	-35.0^{+15}_{-10}	\emptyset	$1.8^{+0.4}_{-0.3}$	1.105

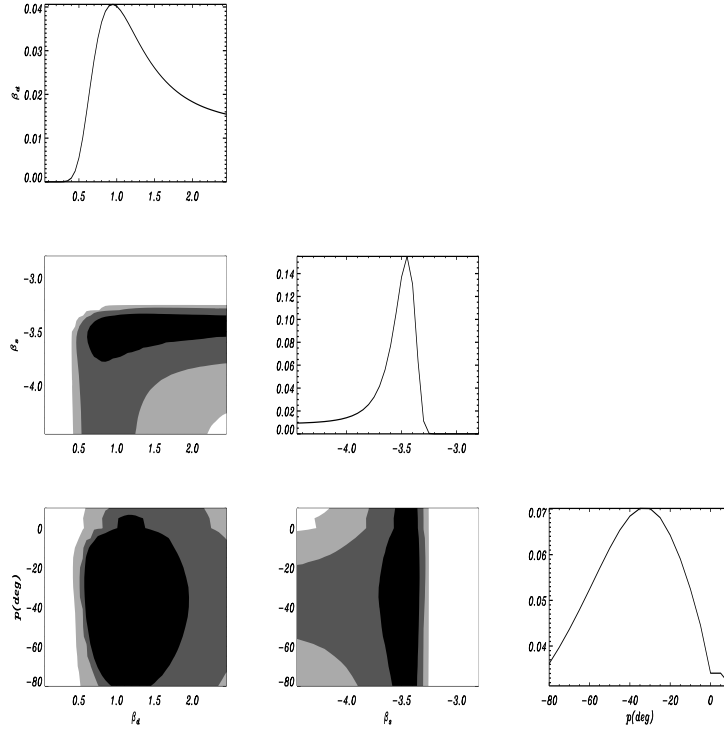


Figure 1: Combined 1 and 2D marginalized likelihood, using all the WMAP channels, for the parameters A_{turb} , β_s , β_d and p assuming no turbulent magnetic field component. We present the 68.8% (dark), 95.4% (dark grey) and 98% (grey) confidence level contours.

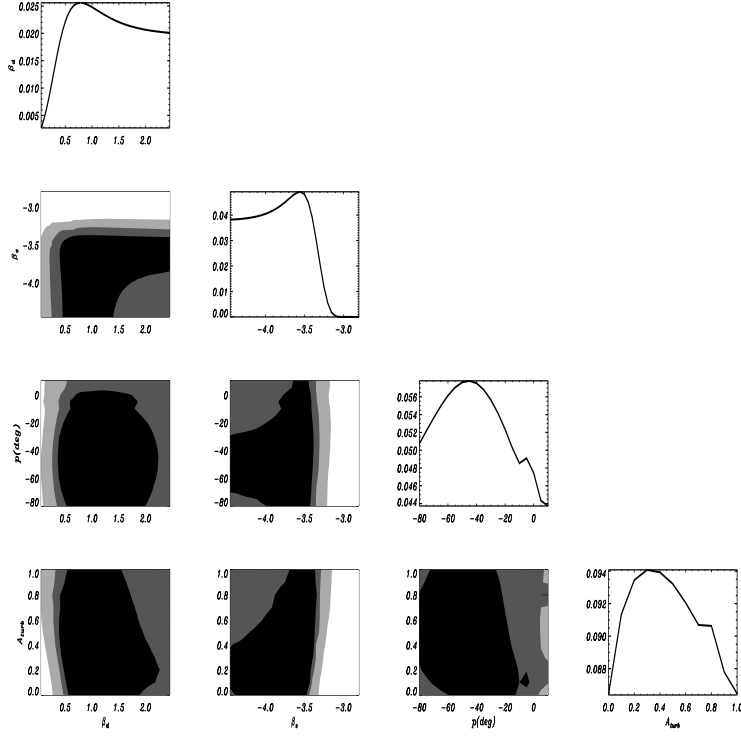


Figure 2: Combined 1 and 2D marginalized likelihood, using all the WMAP channels, for the parameters A_{turb} , β_s , β_d and p including a turbulent magnetic field. We present the 68.8% (black), 95.4% (dark grey) and 98% (grey) confidence level contours.

determination of the degree of polarization and of the dust spectral index is not possible given the available data. Indeed, both parameters act as multiplicative factors. In order to discriminate between them we would need a larger frequency coverage and sampling. The β_s parameter is well constrained at the WMAP frequencies, with a best-fit value of $\beta_s = -3.4^{+0.2}_{-0.5}$, using all the frequency bands and it is consistent across the frequency range. This result is consistent at the 1σ with the results obtained by Fauvet et al. (2011); Gold et al. (2009, 2011); Page et al. (2007); Sun et al. (2008); Jansson et al. (2009).

For the WMAP data we computed the likelihood for the full sky, inside and outside the WMAP processing mask. In the case of β_s , the results obtained inner and outer the mask are consistent with those from the full sky analysis within the error bars. Thus, we can conclude that the spectral variations are smaller than the error bars in the determination of β_s . This seems to be consistent with the results from Gold et al. (2009, 2011) which found that the synchrotron spectral index is relatively constant (with respect to our error bars) across the sky but for the Galactic plane where they found a significant increase. Although the uncertainties on the dust spectral index are much larger our results seem to be consistent with those in Planck-Collaboration (2011b) that favor a larger dust spectral index at high Galactic latitudes.

The constraints on the parameters of the polarized Galactic emission model including a turbulent magnetic field component are presented in Table 3 for the WMAP and ARCHEOPS data. As above, the best-fit parameters of

Table 3: Best-fit parameters for the models of the Galactic polarized emissions including a MLS Galactic magnetic field and a turbulent magnetic field. The χ^2 are given by degree of freedom.

channel	A_{turb}	p	β_s	β_d	χ^2_{min}
Ka	0.3 ± 0.2	-45^{+27}_{-13}	$-3.55^{+0.2}_{-0.5}$	$0.4^{+1.0}_{-0.2}$	13.081
Q	$0.8^{+0.1}_{-0.4}$	-40^{+25}_{-20}	$-3.55^{+0.2}_{-0.5}$	$0.7^{+0.8}_{-0.4}$	4.554
V	< 0.9 (95.4 % CL)	0^{+5}_{-40}	$-3.6^{+0.3}_{-0.4}$	$1.25^{+0.6}_{-0.3}$	1.530
W	$0.8^{+0.1}_{-0.4}$	-5^{+7}_{-37}	$-3.4^{+0.3}_{-0.5}$	$1.6^{+0.4}_{-0.8}$	1.463
all	< 0.5 (95.4 % CL)	-30^{+15}_{-17}	$-3.55^{+0.2}_{-0.5}$	$1.2^{+0.4}_{-0.3}$	20.0
ARCHEOPS 353 GHz	< 2.25 (95.4 % CL)	-20^{+80}_{-50}	\emptyset	$1.8^{+0.7}_{-0.9}$	1.98

the model are consistent from 30 to 353 GHz but the constraints are much more looser. In particular, the relative amplitude of the turbulent component, A_{turb} , is poorly constrained although the data do not seem to favour a strong turbulent component. We present on Figure 2 the combined marginalized likelihood at 1 and 2D using all the WMAP data. We present the 68.8% (black), 95.4% (dark grey) and 98% (grey) confidence level contours.

Figures 3 and 4 compare the Q (top) and U (bottom) Stokes parameter maps obtained from the best-fit parameters (right) to the WMAP Ka and W band maps (left), respectively. The maps are presented in μK_{RJ} units. At 33 GHz the synchrotron emission dominates the signal and the data is well represented by the model. However, at 94 GHz thermal dust emission dominates the signal. This can be observed both on the Q and U maps, although the latter is too noisy for a clear detection of thermal dust emission.

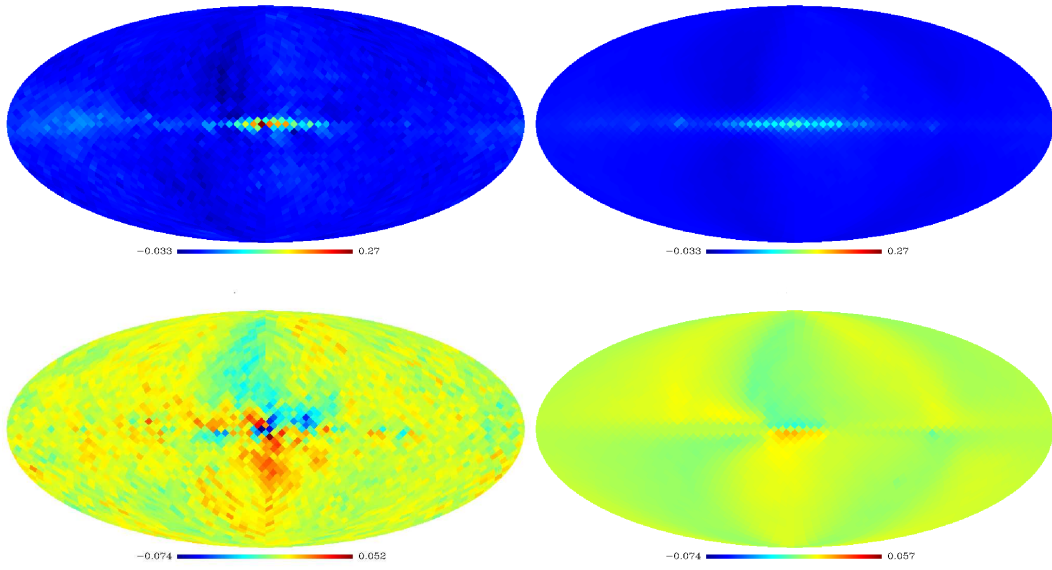


Figure 3: Maps (in μK_{RJ}) for the polarization Q (*top*) and U(*bottom*) Stokes parameters at 33 GHz for the WMAP 5 years data (*left*), and or the best-fit parameters model of the polarized foreground emissions (*right*) .

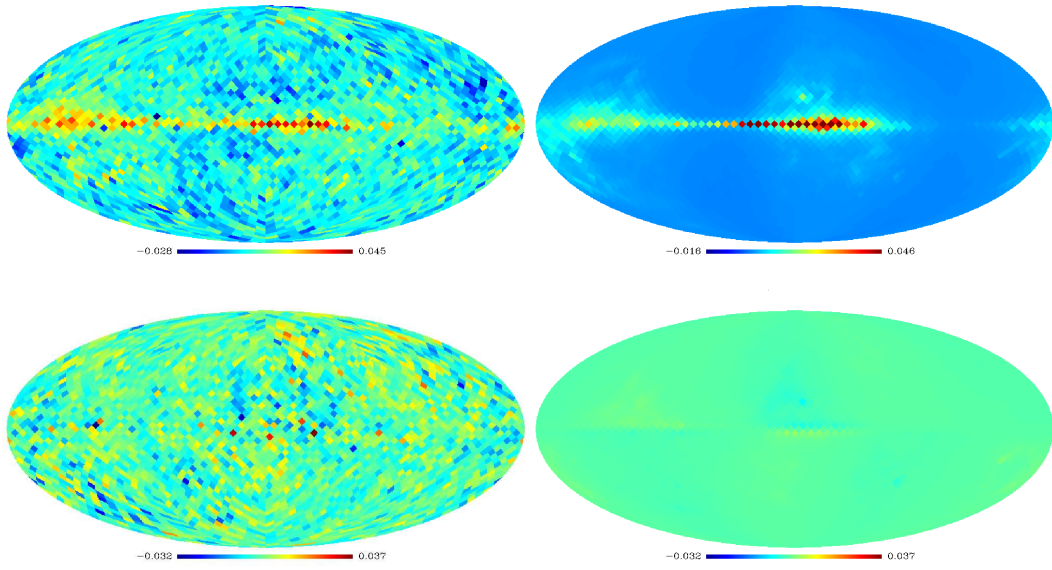


Figure 4: Maps (in μK_{RJ}) for the polarization Q (*top*) and U (*bottom*) Stokes parameters at 94 GHz for the WMAP 5 years data (*left*), and for the best fit model of the polarized foreground emissions (*right*) .

7. Conclusions

We proposed in this paper an extended study of the polarized Galactic diffuse emissions presented in Fauvet et al. (2011). We have constructed coherent models of these two foreground emissions based on a 3D representation of the Galactic magnetic field and of the distributions of relativistic electrons and dust grains in the Galaxy. For the Galactic magnetic field we considered a modified logarithmic spiral model for the large-scale regular component, plus a turbulent one. The relativistic electrons and dust grains distributions have been modeled with exponentials peaking at the Galactic center.

We performed a likelihood analysis to compare the available WMAP and ARCHEOPS data to a set of models obtained by varying the pitch angle of the regular magnetic field, the relative amplitude of the turbulent magnetic field as well as the extrapolation spectral indices for the synchrotron and thermal dust emissions. From this analysis, we observe that the best-fit parameters are compatible across the frequency range explored, indicating that the polarized sky emission at the different frequencies are of the same nature. Using the full data set, we have been able to set constraints on the pitch angle, $p = -30^{+15}_{-17}$ degrees. The best-fit value for the spectral index of the synchrotron emission, $\beta_s = -3.45^{+0.2}_{-0.5}$, is lower but compatible with other values found in the literature (see for example Kogut et al. (2007); Gold et al. (2009)). This low spectral index indicates that the synchrotron emission observed at microwave frequency is produced by relativistic electrons with an steep energy spectrum (spectral index $p = 4$). An upper limit on the relative amplitude of the turbulent component is obtained although it seems that

this turbulent part is not required to reproduce the microwave data at large angular scales. However, we only accounted here for a statistically isotropic turbulent component and we did not for the ordered turbulent component which in our case can not be distinguished from the regular component.

From above we can conclude that a simple model of the polarized Galactic diffuse foreground emission including synchrotron and thermal dust can account for the observed sky emission in the frequency range from 30 to 353 GHz at large angular scales. This is of great interest for the analysis of PLANCK satellite mission data, as PLANCK will measure the polarized CMB anisotropies in the frequency range from 70 to 217 GHz and we expect the foreground emissions to be dominant at large angular scales (Gold et al., 2011; Fauvet et al., 2012).

References

- Baumann, D. e., 2009. In: AIP Conf.Proc. AIP, p. 1141.
- Bennett, C., Halpern, M., Hinshaw, G., Jarosik, N., Kogut, A., Limon, N., Meyer, S., Page, L., Spergel, L., 2003. ApJS148, 1.
- Benoît, A., Ade, P., Amblard, A., Ansari, R., Aubourg, E., Bargout, S., Bartlett, J. G., Bernard, J.-P., Bhatia, R. S., Blanchard, A., 2004. A & A 424, 571.
- Benoît, A., Ade, P., Amblard, A., Ansari, R., Aubourg, E., Bargout, S., Bartlett, J. G., Bernard, J.-P., Bhatia, R. S., Blanchard, A., Bock, J., Boscaleri, A., Bouchet, F., Bourrachot, A., Camus, P., Couchot, F.,

- de Bernardis, P., Delabrouille, J., Desert, F.-X., Doré, O., Douspis, M., Dumoulin, L., Dupac, X., Filliatre, P., Fosalba, P., Ganga, G., Gannaway, F., Gautier, B., Giard, M., Giraud-Heraud, Y., Gispert, R., Guglielmi, L., Hamilton, J., Hanany, S., Henrot-Versille, S., Kaplan, J., Lagache, G., Lamarre, J.-M., Lange, A., Macias-Perez, J., Madet, K., Maffei, B., C., M., 2003. *A & A* 399, 19.
- Betoule, M., Pierpaoli, E., Delabrouille, J., Le Jeune, M., Cardoso, J.-F., 2009. *A&A* 503, 691B.
- Boulanger, F., Abergel, A., Bernard, J.-P., Burton, W. B., Désert, F.-X., Hartmann, D., Lagache, G., Puget, J.-L., 1996. *A&A* 312, 181.
- Burigana, C., Destri, C., de Vega, H. J., Gruppuso, A., Mandolesi, N., Natoli, P., Sanchez, N. G., 2010. *ApJ* 724, 588.
- Burn, B. J., 1966. *MNRAS* 133, 67B.
- Drimmel, R., Spergel, D., 2001. *ApJ* 556, 181.
- Efstathiou, G., Gratton, S., 2009. *JCAP* 6, 11.
- Efstathiou, G., Gratton, S., Paci, F., 2009. *MNRAS* 397, 1355.
- Eisenhauer, F., Schodel, R., Genzel, R., Ott, T., Tecza, M., Abuter, R., Eckart, A. and Alexander, T., 2003. *ApJ* 597, L121.
- Fauvet, L., Macías-Pérez, J. F., Aumont, J., Désert, F. X., Jaffe, T. R., Banday, A. J., Tristram, M., Waelkens, A. H., Santos, D., Feb. 2011. Joint 3D modelling of the polarized Galactic synchrotron and thermal dust foreground diffuse emission. *A&A* 526, A145.

- Fauvet, L., Macías-Pérez, J. F., Jaffe, T. R., Banday, A. J., Désert, F.-X., Santos, D., Jan. 2012. Expected constraints on the Galactic magnetic field using PLANCK data. ArXiv e-prints.
- Finkbeiner, D. P., Davis, M., Schlegel, D., J., 1999. ApJ524, 867.
- Gold, B., Odegard, N., Weiland, J., Hill, R., Kogut, A. Bennett, C., Hinshaw, G., Chen, X., Dunkley, J., Halpern, M., Jarosik, N., Komatsu, E. Larson, D., Limon, M., Meyer, S., Nolta, M., Page, L., Smith, K., Spergel, D., Tucker, G.S. Wollack, E., Wright, E., 2011. ApJSS 192, 15.
- Gold, B., Odegard, N., Weiland, J. L., Hill, R. S., Kogut, A., Bennett, C., Hinshaw, G., Chen, X., Dunkley, J., Halpern, M., Jarosik, N., Komatsu, E., Larson, D., Limon, M., Meyer, S., Nolta, M., Page, L., Smith, K., Spergel, D., Tucker, G., Wollack, E., Wright, E., 2009. ApJS180, 265.
- Gòrski, K., Hivon, E., Banday, A., Wandelt, B. D., Hansen, F. K., Reinecke, M., Bartelmann, M., 2005. ApJ622, 759.
- Han, J. L., Ferrière, K., Manchester, R. N., 2004. A&A610, 820–826.
- Han, J. L., Manchester, R., Lyne, A., Qiao, G. J., van Straten, W., 2006. A&A642, 868.
- Haslam, C., Salter, C., Stoffel, H., Wilson, W. E., 1982. A&AS47, 1.
- Hinshaw, G., Nolta, M., Bennett, C., Bean, R., Doré, O., Greason, M. R., Halpern, M., Hill, R. S., Jarosik, N., Kogut, A., 2007. ApJS170, 288.
- Hinshaw, G., Weiland, J., Hill, R., Odegard, N., Larson, D., Bennett, C., Dunkley, J., Gold, B., Greason, M., Jarosik, N., Komatsu, E., Nolta, M.,

- Page, L., Spergel, D., Wollack, E., Halpern, M., Kogut, A., Limon, R., Meyer, S., Tucker, G., Wright, E., 2009. ApJS180, 225.
- Jaffe, T., Leahy, J., Banday, A., Leach, S., Lowe, S., Wilkinson, A., 2010. MNRAS 401, 1013.
- Jansson, R., Farrar, G., Waelkens, A., Ensslin, T., 2009. JCAP 7, 21.
- Kobayashi, S., Mészáros, P., Zhang, B., Jan. 2004. A Characteristic Dense Environment or Wind Signature in Prompt Gamma-Ray Burst Afterglows. ApJL601, L13–L16.
- Kogut, A., Dunkley, J., Bennett, C., Doré, O., Gold, B., Halpern, M., Hinshaw, G., Jarosik, N., Komatsu, E., Nolte, M., Odegard, N., Page, L., Spergel, D. N., Tucker, G. S., Weiland, J. L., Wollack, E., Wright, E. L., 2007. ApJ665, 355.
- La Porta, L., Burigana, C., Oct. 2006. A multifrequency angular power spectrum analysis of the Leiden polarization surveys. A&A457, 1–14.
- La Porta, L., Burigana, C., Reich, W., Reich, P., Aug. 2006. An angular power spectrum analysis of the DRAO 1.4 GHz polarization survey: implications for CMB observations. A&A455, L9–L12.
- La Porta, L., Burigana, C., Reich, W., Reich, P., Mar. 2008. The impact of Galactic synchrotron emission on CMB anisotropy measurements. I. Angular power spectrum analysis of total intensity all-sky surveys. A&A479, 641–654.

Leach, S. M., Cardoso, J.-F., Baccigalupi, C., Barreiro, R., Betoule, M., Bobin, J., Bonaldi, A., Delabrouille, J., de Zotti, G., Dickinson, C., Eriksen, H., González-Nuevo, J., Hansen, F., Herranz, D., LeJeune, M., López-Caniego, M., Martínez-González, E., Massardi, M., Melin, J.-B., Miville-Deschênes, M.-A., Patanchon, G., Prunet, S., Ricciardi, S., Salerno, E., Sanz, J., Starck, J.-L., Stivoli, F., Stolyarov, V., Stompor, R., Vielva, P., 2008. *A&A*491, 597.

Limon, M., Barnes, C., Bean, R., Bennett, C., Doré, O., Dunkley, J., Gold, B., Greason, M., Halpern, R., Hill, G., Hinshaw, G., Jarosik, N., Kogut, A., Komatsu, E., Landsman, D., Larson, D., Limon, M., Meyer, S., Nolta, M., Odegard, N., Page, L., Peiris, H., Spergel, D., Tucker, G., Verde, L., Weiland, J., Wollack, E., Wright, E., 2009. *Wilkinson Microwave Anisotropy Probe (WMAP): Five-Year Explanatory Supplement*. M. Limon et al.

Lyne, A., Smith, F., 1989. *MNRAS* 237, 533.

Lyth, D. H., 1984. *Phys. Lett. B* 147, 403.

Macías-Pérez, J., Lagache, G., Maffei, B., Ade, P., Amblard, A., Ansari, R., Aubourg, E., Aumont, J., Bargout, S., Bartlett, J., Benoit, A., Bernard, J.-P., Bhatia, R., Blanchard, A., Bock, J., Boscaleri, A., Bouchet, F., Bourrachot, A., Camus, P., Cardoso, J.-F., Couchot, F., de Bernardis, P., Delabrouille, J., Desert, F., Doré, O., Douspis, M., Dumoulin, L., Dupac, X., Filliatre, P., Fosalba, P., Ganga, K., Gannaway, F., Gautier, B., Girard, M., Giraud Heraud, Y., Gispert, R., Guglielmi, L., Hamilton, J.-C., Hanany, S., Henrot Versille, S., Hristov, V., Kaplan, J., Lamarre, J.-M., Lange, A., Madet, K., Magneville, C., Marrone, D., Masi, S., Mayet, F.,

- Murphy, J., Naraghi, F., Nati, F., Patanchon, G., Perdereau, O., Perrin, G., Plaszczyński, S., Piat, M., Ponthieu, N., Prunet, S., Puget, J., Renault, C., Rosset, C., Santos, D., 2007. A&A467, 1313.
- Neugebauer, G., Habing, H. J., van Duinen, R., Aumann, H. H., Baud, B., Beichman, C. A. and Beintema, D. A., Boggess, N., Clegg, P. E., de Jong, T., 1984. ApJ278, 1.
- Page, L., Barnes, C., Hinshaw, G., Spergel, D., Weiland, J., Wollack, E., Bennett, C., 2003. ApJS148, 39.
- Page, L., Hinshaw, G., Komatsu, E., Nolta, M. R., Spergel, D. N., Bennett, C. L., Barnes, C., Bean, R., Doré, O., Dunkley, J., Halpern, M., Hill, R., Jarosik, N., Kogut, A., Limon, M., Meyer, S., Odegard, M., Peiris, H., Tucker, G., Verde, L., Weiland, J., Wollack, E., Wright, E., 2007. ApJS170, 335.
- Peiris, H., Komatsu, E., Verde, L., 2003. ApJS148, 213.
- Planck-Collaboration, 2005. Planck: the Scientific Program. Vol. 1. ESA-SCI.
- Planck-Collaboration, 2011a. Planck early results 1 : The planck mission. A& A accepted 536, 1.
- Planck-Collaboration, 2011b. Planck early results 24 : Dust in the interstellar medium and the galactic halo. A&A 536, 24.
- Planck-Collaboration, 2011c. Planck early results: All sky temperature and dust optical depth from planck and iras: Constraints on the dark gas in our galaxy. A&A submitted 536, 19.

- Ponthieu, N., Macías-Pérez, J., Tristram, M., 2005. *A&A*444, 327.
- Reid, M., Brunthaler, A., 2005. In: Reid, J. R. . M. (Ed.), *ASP Conf. Ser. 340, Future Directions in High Resolution Astronomy: The 10th Anniversary of the VLBA*. ASP, San Fransisco, p. 253.
- Rybicki, G., Lightman, A., 1979. *Radiative Process in Astrophysics*. Wiley-Interscience, New York.
- Schlegel, D. J., Finkbeiner, D., Davis, M., 1998. *ApJ*500, 525.
- Sun, X., Reich, W., Waelkens, A., Ensslin, T., 2008. *A&A*477, 573.
- Tauber, J. A., Mandolesi, N., Puget, J. L., Bouchet, F., 2010. *A&A* 520 (A1).
- Taylor, J. H. J., Cordes, J. M., 1993. *ApJ*411, 674.
- Waelkens, A., Jaffe, T., Reinecke, M., Kitauro, F. S., Ensslin, T., 2009. *A&A*495, 697.